Structure of Graphene Grown on Cu(111): X-Ray Standing Wave Measurement and Density Functional Theory Prediction

Matthew A. Stoodley,[1,2] Luke A. Rochford,[2] Tien-Lin Lee,[2] Benedikt P. Klein,[1,2,*] David A. Duncan,[2,†] and Reinhard J. Maurer[1,3,‡]

[1]Department of Chemistry, University of Warwick, Gibbet Hill Road, CV4 7AL Coventry, United Kingdom
[2]Diamond Light Source, Harwell Science and Innovation Campus, Fermi Avenue, OX11 ODE, Didcot, United Kingdom
[3]Department of Physics, University of Warwick, Gibbet Hill Road, CV4 7AL Coventry, United Kingdom

(Received 17 October 2023; revised 11 March 2024; accepted 2 April 2024; published 7 May 2024)

We report the quantitative adsorption structure of pristine graphene on Cu(111) determined using the normal incidence x-ray standing wave technique. The experiments constitute an important benchmark reference for the development of density functional theory approximations able to capture long-range dispersion interactions. Electronic structure calculations based on many-body dispersion-inclusive density functional theory are able to accurately predict the absolute measure and variation of adsorption height when the coexistence of multiple moiré superstructures is considered. This provides a structural model consistent with scanning probe microscopy results.

DOI: 10.1103/PhysRevLett.132.196201

Over the last 20 years, few materials and interfaces have garnered more attention than the graphene-metal interface [1,2]. Many different synthesis routes have been devised for graphene on metal substrates [3], and detailed structural and electronic characterization of graphene has been reported on various single crystal metal surfaces, including: Ir(111) [4], SiC(0001) [5–7], Ni(111) [8], and Cu(111) [9]. When weakly adsorbed [10,11], the electronic properties of graphene are preserved, but when strong interactions are present these properties can be lost [12].

X-ray standing waves (XSWs), photoelectron diffraction, and density functional theory (DFT) have been used to characterize the adsorption height (d) and corrugation (Δd) of graphene on Ir(111) [4], Ni(111) [8], SiC(0001) [5,6], and H-intercalated SiC(0001) [6]. These examples exhibit a significant range of intralayer corrugations (0.02–1.0 Å; see Table I and Table S1 in the SM [13]), exemplifying the substrate dependence of graphene's structure.

Strong graphene-metal interactions can lead to a strained, commensurate graphene overlayer [35]. More commonly, the lattice mismatch between the two materials leads to moiré patterns [35,36] that manifest as periodic modulations of tunneling current in scanning tunneling microscopy (STM), e.g., graphene-Ir(111) [4] and graphene-SiC(0001) [37]. In particular, graphene on Cu(111) exhibits many coexisting moiré patterns. A small subset has previously been identified, with associated moiré rotational angles (angle between the graphene and substrate lattices) [9,11,38–40]. STM and noncontact atomic force microscopy (nc-AFM) alone cannot unambiguously separate structural, mechanical, and electronic corrugation effects that contribute to the moiré pattern. Though, nc-AFM indicates a weak structural corrugation (0.25 Å) for a singular graphene-Cu(111) moiré pattern [41], but little is understood about height variations between different moiré patterns. By contrast, structural corrugation of graphene on Ir(111) and SiC(0001) has been evidenced by XSW and DFT calculations [4–6].

The adsorption height of graphene on Cu(111) has not been unambiguously determined. Only two results exist in

TABLE I. Coherent fractions (f_{111}), adsorption heights (d) above a bulk truncated surface, and corrugations (Δd) for graphene on Ni(111) [8], SiC(0001) [5,6], H-intercalated SiC(0001) [H-SiC(0001)] [6], Ir(111) [4], and graphene on Cu(111). Uncertainties on the last significant figures are given in brackets. DFT functionals used: SiC(0001) [5]: vdW-TS [33], Ni(111) [8]: PBE, Ir(111) [4]: vdW-DF [34], Cu(111): HSE06 + MBD-NL (Fig. 3). The Ni(111) experimental results were obtained by photoelectron diffraction, all other systems by XSW.

Substrate	f_{111}	d (Å)	Δd (Å)	DFT d (Å)
Ni(111) [8]	⋯	2.17	0.04	2.11
SiC(0001) [5,6]	0.7(3)	5.80	0.45	5.76
H-SiC(0001) [6]	0.75	4.22(4)	0.02(6)	4.16
Ir(111) [4]	0.74(4)	3.38(4)	1.0(2)	3.41
Cu(111)	0.77(2)	3.24(2)	0.00–0.12	3.04–3.29

Published by the American Physical Society under the terms of the Creative Commons Attribution 4.0 International license. Further distribution of this work must maintain attribution to the author(s) and the published article's title, journal citation, and DOI.

the literature: 3.13 ± 0.02 Å [42] in XSW for graphene formed from nanoribbons and 3.34 ± 0.06 Å [43] in positron diffraction. Numerous theoretical studies have reported the adsorption height of graphene on Cu(111), both for commensurate and strained structures [44–49] and near commensurate superstructures [40,50]. However, different exchange-correlation (XC) approximations yield wildly different adsorption heights (2.21–5.54 Å [44–49]). Without accurate experimental reference data, the reliability of first principles predictions cannot be directly assessed, limiting the development of DFT XC approximations.

In this Letter, we report XSW measurements of graphene grown in ultrahigh vacuum on a Cu(111) single crystal via chemical vapor deposition of a novel precursor [11]. We predict structures based on state-of-the-art long-range many-body dispersion-inclusive DFT calculations that consider the experimental moiré superstructures. The calculations accurately predict the vertical height of carbon atoms within the graphene overlayer and show that including multiple moiré superstructures to accurately model XSW measurements is crucial.

Graphene was grown *in situ* on Cu(111) under ultrahigh vacuum conditions following the methodology in Ref. [11]. Atomically clean Cu(111) samples were prepared by cycles of sputtering (Ar^+) and annealing (~1000 K). The sample, held at 1000 K, was exposed to a flux of azupyrene molecules (~320 K). X-ray photoelectron spectroscopy, low energy electron diffraction, Raman, and angle-resolved photoemission spectroscopy confirm the growth of high-purity, pristine graphene [11]. All samples were of sub-monolayer coverage and were measured at 300 K. Further experimental and computational details are described in the SM [13].

The Cu(111) Bragg reflection at normal incidence was used to create an XSW field at a photon energy of 2.63 keV. At the Bragg condition, the antinodes of the XSW lie halfway between the Bragg diffraction planes (BDPs) [51]. Increasing the photon energy shifts the antinodes toward these BDPs. Thus, the adsorbed graphene will experience varying photon flux as a function of its adsorption height as the photon energy is varied, resulting in a modulation in the photoelectron yield. This modulation is fitted with two dimensionless parameters [52]: the coherent fraction, f_{111}, and the coherent position, p_{111}. f_{111} is related to the order of the system, p_{111} describes the position of the atoms relative to the BDPs [51].

The acquired C 1s XSW data for graphene on Cu(111) is shown in Fig. 1(a). The fitted f_{111} for these data is 0.77 ± 0.02, discussed in detail below. The resulting p_{111} is 0.55 ± 0.01 and corresponds to a d of 3.24 ± 0.02 Å. This adsorption height is close to the sum of the van der Waals radii of copper and carbon (3.1 Å [53,54]), indicating that long-range dispersion interactions dominate the graphene-Cu(111) interface.

A positron diffraction study of graphene on Cu(111), found an adsorption height of 3.34 ± 0.06 Å [43], slightly larger than the XSW result. Positron diffraction is still a maturing technique and requires an iterative comparison to structural models. In that work, only a single (1×1) unit cell of graphene was considered, thus only neighbor-neighbor buckling was probed, excluding long-range corrugation.

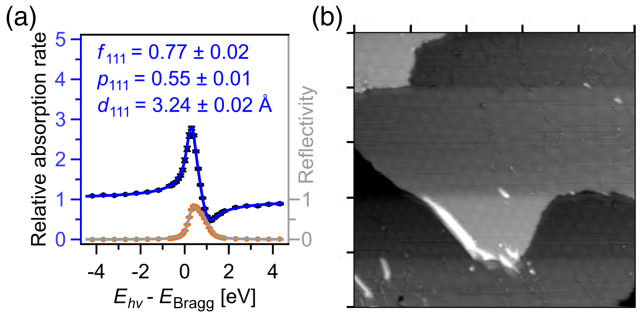

FIG. 1. (a) C 1s XSW of graphene on Cu(111). The experimental data points are represented by the black and orange markers. The blue and grey curves represent the fits of the C 1s photoelectron yield and the X-ray reflectivity, respectively. The blue and grey y-axes correspond to the photoelectron yield and reflectivity, respectively. (b) STM image (with an applied flatting function) of the graphene sample featuring multiple moiré patterns, area: 100×100 nm^2, tunneling voltage: 1.2 V, current: 150 pA.

Graphene formed by annealing of preadsorbed graphene-like nanoribbons [42] had a f_{111} of 0.61 and a p_{111} of 0.49, significantly lower than values found in this study. The binding energy of the main peak in the C 1s x-ray photoelectron spectrum of the nanoribbon is effectively identical to that of graphene, making their separation in the XSW difficult. However, the difference in the results of these two works could be fully rationalized by a proportion (~20%) of the nanoribbons remaining unreacted.

Our measured f_{111} for graphene on Cu(111) is comparable to that of graphene on Ir(111) (0.74 ± 0.04) [4] and h-BN on Cu(111) (B: 0.65 ± 0.03; N: 0.71 ± 0.02) [55]. For both of these systems the deviation of f_{111} from unity was ascribed to a corrugation of the layers [4,55]. The measured adsorption height of graphene on Cu(111) is only slightly lower than h-BN on Cu(111) ($d = 3.37$–3.39 ± 0.04 Å) [55], and graphene on Ir(111) ($d = 3.38 \pm 0.04$ Å) [4]. To probe the possible role of corrugation in these films, we turn to DFT calculations.

Several studies have assessed the ability of different XC functional approximations to predict the adsorption height of graphene on Cu(111) using a hypothetical, commensurate (1×1) model of the graphene-metal interface [44–49]. In Fig. 2, we summarize these literature results. Local density approximation (LDA) predictions lie between 2.5 and 3.25 Å. We note that LDA overbinding can lead to fortuitous adsorption heights that appear to be consistent with physisorption [56]. Perdew-Burke-Ernzerhof (PBE) and revised PBE (RPBE) functionals based on the generalized gradient approximation (GGA) mitigate LDA

overbinding and effectively predict no binding, as they explicitly neglect long-range dispersion interactions. Predictions with van der Waals correlation functionals (vdW-DF) provide heights in the range of 3.26 and 3.80 Å [45,47,48]. Random phase approximation (RPA) calculations based on underlying PBE DFT calculations and combined with exact exchange (RPA + EXX) [57–59] predicted an adsorption height of 3.25 Å [46]. This was later corrected to 3.09 Å [47]. Unfortunately, RPA + EXX remains computationally intractable for systems with hundreds of atoms.

A similarly broad scatter of predictions across different XC functionals has been reported for other metal-organic interfaces, e.g., benzene [60] and PTCDA [61] on Ag(111); and naphthalene on Cu(111) [62]. For physisorption at molecule-metal interfaces, long-range dispersion correction schemes such as the Tkatchenko-Scheffler vdW^{surf} [63], the many-body dispersion (MBD [64,65]), and the nonlocal MBD (MBD-NL [66]), coupled with either PBE [67] or Heyd-Scuseria-Ernzerhof (HSE06 [68]), have yielded excellent predictions [56,69,70]. The pairwise additive vdW^{surf} scheme explicitly captures the screening of interactions that affect the distance dependence of long-range dispersion at conducting substrates. The MBD-NL method accounts for the collective many-body response and screening effects mitigating overbinding that is often observed with pairwise additive methods. In combination with HSE06, which provides an accurate representation of the Pauli repulsion between closed shell adsorbates and the surface, these methods provide computationally efficient and scalable alternatives to explicit long-range correlation functionals and are used herein to model the experimental results.

To directly compare MBD-NL and vdW^{surf} corrected functionals to the literature, we performed calculations of graphene on Cu(111) with a commensurate (1 × 1) surface slab model represented by eight layers of copper (Fig. 2). In previous (1 × 1) calculations, the most stable adsorption configuration had the two symmetrically inequivalent carbon atoms adsorbed directly above the atop and fcc hollow sites (Fig. 2) [46–48,71], which we confirm for the employed functionals. The MBD-NL correction yields better agreement with the experiment, with PBE + MBD-NL within 0.06 Å of the experimental value. The MBD-NL correction yields shallower minima in BE compared to the vdW^{surf} correction. The latter is known to overestimate adsorption energies [60,70]. Unfortunately, no experimental measurement of the adsorption energy for graphene exists.

Figures 2 and S9 in the SM [13] show that PBE + MBD-NL provides a shallow BE well with a slow repulsive onset. By including exact exchange via the range-separated hybrid functional HSE06 + MBD-NL (blue curve in Fig. 2), this is remedied and the minimum is found at a lower adsorption height. A similar behavior has been

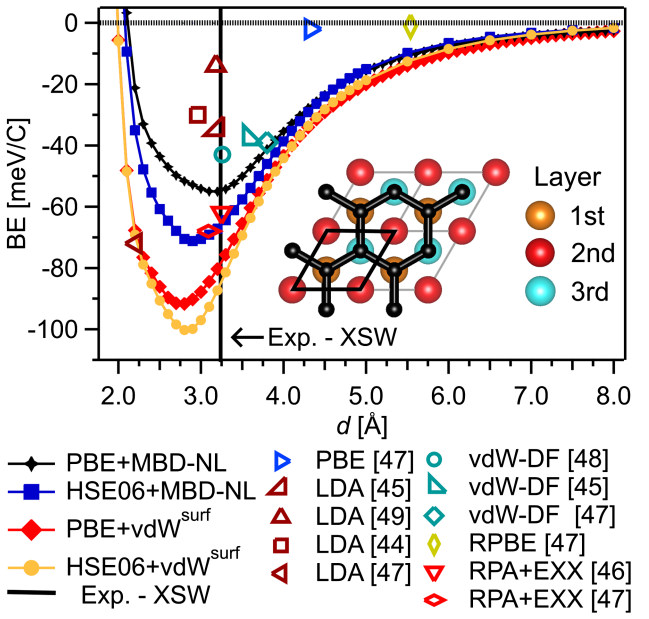

FIG. 2. Binding energy (BE) curve of the commensurate (1 × 1) supercell of graphene on Cu(111), performed with the PBE + MBD-NL, PBE + vdW^{surf}, HSE06 + MBD-NL, and HSE06 + vdW^{surf} calculated here. Functionals used in literature [44–49] are indicated in the figure legend. Here, d values are the height difference between graphene and the surface on which the graphene was optimized. Inset: schematic of (1 × 1) structure. The unit cell indicated by black lines. Carbon atoms, black; copper atoms, see inset.

reported for benzene on Ag(111), where the dispersion-inclusive range-separated hybrid functional provided an improved description of the adsorption height [60].

The RPA + EXX and vdW-DF results for the (1 × 1) structure appear to provide better agreement with the experiment. However, the (1 × 1) model induces considerable strain on the graphene lattice ranging from 3.13% for PBE + MBD-NL to 4.80% for HSE06 + vdW^{surf} (see Tables S6–S9 and Fig. S7 in the SM [13]). A strain larger than ∼1.5% is questionable [72] and, as we will demonstrate below, removing the strain by considering realistic moiré superstructures is key to accurately predicting the adsorption structure.

Several other theoretical works considered the moiré superstructure for this system [40,50,73], but without the benchmark of the quantitative experimental results presented here. We modeled eight representative moiré patterns with a strain between ±1%. These superstructures range in size between 26–314 carbon atoms with periodicities between 0.88 and 3.08 nm. A subset of these superstructures contain periodicities and angles observed in STM measurements [11,40,44]. Further details on the calculated moiré patterns can be found in the SM [13], Tables S3–S9.

Figures 3 and S9–S11 [13] show the relaxed adsorption heights and optimized structures for all eight moiré patterns

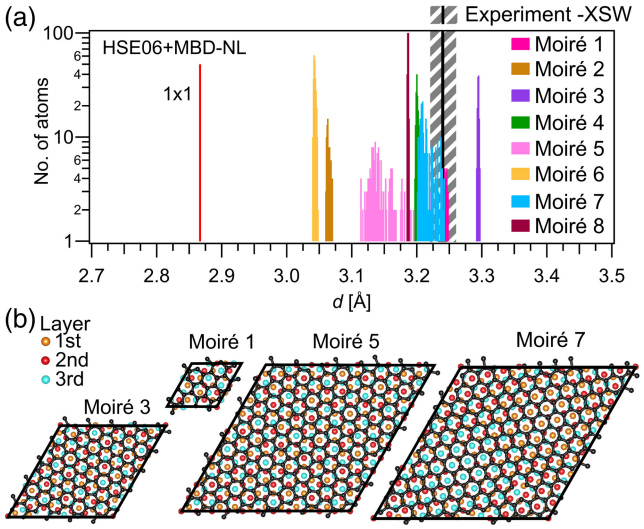

FIG. 3. (a) Histogram of adsorption heights in each moiré pattern for the HSE06 + MBD-NL functional compared to experiment. Here, d values are the height difference between graphene and a projected bulklike truncation of the Cu surface. Tables S6 and S7 in the electronic SM [13] summarize the adsorption heights with respect to the relaxed Cu surface. Nb: the 1×1 cell contains two atoms. The red bar is increased here for visual clarity. (b) Optimized structures of a subset of the studied moiré patterns calculated with HSE06 + MBD-NL. The full set of moiré structures are shown in Fig. S11.

with PBE + MBD-NL and HSE06 + MBD-NL and the vdW^{surf} methods. In the following, we will focus on the MBD-NL results. For the PBE + MBD-NL prediction, the mean adsorption height in the (1×1) model was 3.18 Å, whereas the different moiré superstructures range from 3.22 to 3.33 Å. For HSE06 + MBD-NL, this effect is starker with the (1×1) unit cell yielding a height of 2.87 Å and the moiré structures ranging from 3.04 to 3.29 Å. Thus, relieving the strain on the graphene lattice has a strong effect on the predicted adsorption height.

Figure 3 shows that the average adsorption height and corrugation (defined as the difference between highest and lowest atom) of each moiré superstructure differ significantly with rotational alignment to the substrate (see Tables S6–S7 in the SM [13]). Some moiré superstructures show virtually no corrugation (e.g., moiré 2, 3, and 6), while others exhibit corrugation beyond ±0.11 Å (e.g., moiré 5 and 7). Both functionals agree on which superstructures show more or less corrugation. Generally, as the angle of rotation increases, the corrugation decreases (see Fig. S13 in the SM [13]), a behavior previously reported in the literature [40,73]. The corrugation does not directly correlate with the magnitude of lattice strain in the graphene layer.

PBE + MBD-NL moiré superstructures exhibit adsorption heights that are predominantly larger (3.22–3.33 Å) than the experimental value (3.24 ± 0.02 Å). Predictions with the HSE06 + MBD-NL functional show adsorption heights that are predominantly lower (3.04–3.29 Å) than the experimental value. As all BE curves are anharmonic, we expect 0 K DFT structure predictions to provide lower bounds on the adsorption heights measured at finite temperature (300 K) and that finite temperature effects will, at least to a minor extent, increase the average adsorption heights [70]. If finite temperature effects are considered, the adsorption heights predicted by PBE + MBD-NL would further overestimate, whereas HSE06 + MBD-NL heights would be closer to, the experiment.

Up to now, we have only compared the average adsorption heights from the calculations to the XSW results. We now analyze the measured coherent fraction (0.77 ± 0.02) that captures the spread of adsorption heights. The interpretation of coherent fractions is complicated by a convolution of dynamical (i.e., thermal vibrations) and static structural variations (i.e., corrugation).

To explain the measured f_{111} solely by thermal vibrations requires a root mean square vibrational amplitude (rms-va) of 0.24 Å. We performed phonon band structure calculations on freestanding graphene to estimate the scale of dynamic effects on the rms-va at 300 K (further details in Sec. 4 of the SM [13]). We predict an average rms-va of 0.12 Å, similar to the experimental value measured for bulk graphite (0.11 Å [74]). Thus, the dynamical variation of adsorption heights is not large enough to explain the reduced f_{111} observed in the XSW experiments.

The static corrugation of graphene on Cu across a single moiré pattern can be estimated from STM and nc-AFM. Note that apparent heights in both STM and nc-AFM can be ambiguous, and are used here as an indicative estimate of the scale of the static corrugation. Prior measurements show apparent corrugations of 0.15–0.35 Å in STM [9,40] and 0.25 Å in nc-AFM [41]. The apparent moiré corrugation extracted from our own STM measurements (0.10–0.48 Å; see Sec. 2, Table S2 in the SM [13] for details) agree well with the literature values. The largest DFT predicted corrugation (HSE06 + MBD-NL) is 0.12 Å, similar to the smallest corrugations seen in STM measurements.

To draw comparisons between the rms-va needed to explain the XSW results, experimental STM and nc-AFM data, and the DFT calculations, we convert the corrugations into root mean square displacement values (rms-d). Assuming an rms-va of 0.12 Å, an rms-d of 0.21 Å would be required to explain the measured f_{111}. For the STM and nc-AFM data, we assumed a sinusoidal distribution of the adsorption heights, while we calculated the rms-d directly for the DFT moiré structures (see Sec. 3, Tables S6–S9 of the SM [13] for details). The rms-d of nc-AFM (0.0625 Å [41]), our STM (0.024–0.120 Å), and DFT (0.001–0.031 Å), are all much smaller than the rms-d required to fully account for the reduction of the f_{111} in the XSW results. Therefore the reduced f_{111} also cannot be explained

by the static variations of the 0 K adsorption heights within one moiré superstructure.

STM [Fig. 1(b) and Refs. [9,38,40]), LEED [11,75], and nc-AFM [41] data show that many different moiré patterns coexist on the surface. Scanning probe measurements, as well as the DFT calculations inherently capture the local structure over a few nanometers, whereas XSW is an area-averaging technique ($\sim 400 \times 400\ \mu m^2$). The XSW analysis therefore contains contributions from different moiré structures, whose variation in adsorption height is greater than their individual corrugations [see Figs. 3(a) and S10 in the SM [13]]. To roughly estimate this effect, we calculate the rms-d that arises from a combination of the two DFT superstructures with the largest adsorption height difference. Assuming a one-to-one mixture yields an rms-d of 0.13 Å, closer to the required 0.21 Å. When combined with the theoretically calculated vibrational rms-va of 0.12 Å, we obtain a f_{111} of 0.87 (see SM [13] for details). As our DFT study only includes comparably small (< 3.1 nm) moiré patterns, a complete set of moiré patterns would likely yield an even larger spread of adsorption heights. Thus, only the combination of dynamical effects of the lattice vibrations and different moiré structures with varying adsorption heights comes close to explaining the reduced f_{111} in the XSW data.

In summary, we report the structural characterization of graphene on Cu(111) with complementary XSW measurements and state-of-the-art dispersion-inclusive DFT calculations. Commensurate (1×1) graphene structures are unreliable structural models to assess the accuracy of existing and new XC approximations to DFT. To fully rationalize the measured coherent positions and coherent fractions, the moiré superstructure of graphene on Cu(111) must be considered. In doing so, DFT predictions with the HSE06 + MBD-NL XC functional are in excellent agreement with experiment. Furthermore, careful consideration of multiple different coexisting moiré superstructures is required to correctly reflect the distribution of adsorption heights. The results will provide valuable reference data for XC functional development and could be applied to graphene on other substrates.

All experimental and computational data has been deposited in the NOMAD online database [76].

The authors acknowledge support via a UKRI Future Leaders Fellowship [MR/S016023/1], a UKRI Frontier grant [EP/X014088/1] (R. J. M.), a DFG Walter Benjamin fellowship [KL-3430/1-1] (B. P. K.), the Analytical Sciences CDT at Warwick and a Diamond studentship (M. A. S.). The authors thank Diamond Light Source for access to beamline I09 (SI25379-4). We acknowledge that the results of this research have been achieved using the DECI resource Mahti based in Finland at CSC with support from the PRACE aisbl (project GRAPHSAC). We acknowledge computational resources from ARCHER2 UK National Computing Service which was granted via the EPSRC-funded HEC Materials Chemistry (EP/L000202/1, EP/R029431/1) and HPC-CONEXS (EP/X035514/1) consortia.

*Corresponding author: kleinbe34@kbsi.re.kr
Present address: Research Center for Materials Analysis, Korea Basic Science Institute, 169-148 Gwahak-ro, Yuseong-gu, Daejeon, Korea [34133].
†Corresponding author: david.duncan@diamond.ac.uk
‡Corresponding author: r.maurer@warwick.ac.uk

[1] K. S. Novoselov *et al.*, Electric field effect in atomically thin carbon films, Science **306**, 666 (2016).
[2] N. A. A. Ghany, S. A. Elsherif, and H. T. Handal, Revolution of Graphene for different applications: State-of-the-art, Surface and Interfaces **9**, 93 (2017).
[3] V. B. Mbayachi, E. Ndayiragije, T. Sammani, S. Taj, E. R. Mbuta, and A. ullah Khan, Graphene synthesis, characterization and its applications: A review, Results Chem. **3**, 100163 (2021).
[4] C. Busse, P. Lazić, R. Djemour, J. Coraux, T. Gerber, N. Atodiresei, V. Caciuc, R. Brako, A. T. N'Diaye, S. Blügel, J. Zegenhagen, and T. Michely, Graphene on Ir(111): Physisorption with chemical modulation, Phys. Rev. Lett. **107**, 036101 (2011).
[5] J. D. Emery, B. Detlefs, H. J. Karmel, L. O. Nyakiti, D. K. Gaskill, M. C. Hersam, J. Zegenhagen, and M. J. Bedzyk, Chemically resolved interface structure of epitaxial graphene on SiC(0001), Phys. Rev. Lett. **111**, 215501 (2013).
[6] J. Sforzini, L. Nemec, T. Denig, B. Stadtmüller, T. L. Lee, C. Kumpf, S. Soubatch, U. Starke, P. Rinke, V. Blum, F. C. Bocquet, and F. S. Tautz, Approaching truly freestanding graphene: The structure of hydrogen-intercalated graphene on 6H − SiC (0001), Phys. Rev. Lett. **114**, 106804 (2015).
[7] S. Goler, C. Coletti, V. Piazza, P. Pingue, F. Colangelo, V. Pellegrini, K. V. Emtsev, S. Forti, U. Starke, F. Beltram, and S. Heun, Revealing the atomic structure of the buffer layer between SiC(0001) and epitaxial graphene, Carbon **51**, 249 (2013).
[8] D. E. Parreiras, E. A. Soares, G. J. P. Abreu, T. E. P. Bueno, W. P. Fernandes, V. E. de Carvalho, S. S. Carara, H. Chacham, and R. Paniago, Graphene/Ni(111) surface structure probed by low-energy electron diffraction, photoelectron diffraction, and first-principles calculations, Phys. Rev. B **90**, 155454 (2014).
[9] L. Gao, J. R. Guest, and N. P. Guisinger, Epitaxial graphene on Cu(111), Nano Lett. **10**, 3512 (2010).
[10] M. Kralj, I. Pletikosić, M. Petrović, P. Pervan, M. Milun, A. T. N'Diaye, C. Busse, T. Michely, J. Fujii, and I. Vobornik, Graphene on Ir(111) characterized by angle-resolved photoemission, Phys. Rev. B **84**, 075427 (2011).
[11] B. P. Klein, M. A. Stoodley, M. Edmondson, L. A. Rochford, M. Walker, L. Sattler, S. M. Weber, G. Hilt, L. B. S. Williams, T.-L. Lee, A. Saywell, R. J. Maurer, and D. A. Duncan, Using polycyclic aromatic hydrocarbons for

graphene growth on Cu(111) under ultra-high vacuum, Appl. Phys. Lett. **121**, 191603 (2022).
[12] A. Grüneis and D. V. Vyalikh, Tunable hybridization between electronic states of graphene and a metal surface, Phys. Rev. B **77**, 193401 (2008).
[13] See Supplemental Material at http://link.aps.org/supplemental/10.1103/PhysRevLett.132.196201 for a description of experimental and computational methods, along with a summary of moiré patterns naming conventions and parameters, which includes Refs. [14–32].
[14] D. P. Woodruff and D. A. Duncan, X-ray standing wave studies of molecular adsorption: Why coherent fractions matter, New J. Phys. **22**, 113012 (2020).
[15] W. Kim, K. Yoo, E. K. Seo, S. J. Kim, and C. Hwang, Scanning tunneling microscopy study on a graphene layer grown on a single-crystal Cu(111) surface by using chemical vapor deposition, J. Korean Phys. Soc. **59**, 71 (2011).
[16] F. Schreiber, K. A. Ritley, I. A. Vartanyants, H. Dosch, J. Zegenhagen, and B. C. Cowie, Non-dipolar contributions in XPS detection of x-ray standing waves, Surf. Sci. **486**, L519 (2001).
[17] M. E. Straumanis and L. S. Yu, Lattice parameters, densities, expansion coefficients and perfection of structure of Cu and of C$u-$In α phase, Acta Crystallogr. Sect. A **25**, 676 (1969).
[18] A. V. Krukau, O. A. Vydrov, A. F. Izmaylov, and G. E. Scuseria, Influence of the exchange screening parameter on the performance of screened hybrid functionals, J. Chem. Phys. **125**, 224106 (2006).
[19] C. J. Fisher, R. Ithin, R. G. Jones, G. J. Jackson, D. P. Woodruff, and B. C. Cowie, Non-dipole photoemission effects in x-ray standing wavefield determination of surface structure, J. Phys. Condens. Matter **10**, L623 (1998).
[20] J. Zegenhagen and A. Kazimirov, *The X-Ray Standing Wave Technique* (World Scientific, Singapore, 2013), pp. 3–35, 10.1142/6666.
[21] V. Blum, R. Gehrke, F. Hanke, P. Havu, V. Havu, X. Ren, K. Reuter, and M. Scheffler, *Ab initio* molecular simulations with numeric atom-centered orbitals, Comput. Phys. Commun. **180**, 2175 (2009).
[22] J. E. Peralta, J. Heyd, G. E. Scuseria, and R. L. Martin, Spin-orbit splittings and energy band gaps calculated with the Heyd-Scuseria-Ernzerhof screened hybrid functional, Phys. Rev. B **74**, 073101 (2006).
[23] F. Birch, Finite elastic strain of cubic crystals, Phys. Rev. **71**, 809 (1947).
[24] M. Hebbache and M. Zemzemi, *Ab initio* study of high-pressure behavior of a low compressibility metal and a hard material: Osmium and diamond, Phys. Rev. B **70**, 224107 (2004).
[25] V. G. Ruiz, W. Liu, and A. Tkatchenko, Density-functional theory with screened van der Waals interactions applied to atomic and molecular adsorbates on close-packed and non-close-packed surfaces, Phys. Rev. B **93**, 035118 (2016).
[26] B. H. Shuai Chen, Yong-Hua Duan, and W.-C. Hu, Structural properties, phase stability, elastic properties and electronic structures of Cu $-$ Ti intermetallics, Philos. Mag. **95**, 3535 (2015).
[27] A. Togo, L. Chaput, T. Tadano, and I. Tanaka, Implementation strategies in PHONOPY and PHONO3PY, J. Phys. Condens. Matter **35**, 353001 (2023).
[28] A. Togo, First-principles phonon calculations with phonopy and PHONO3PY, J. Phys. Soc. Jpn. **92**, 012001 (2023).
[29] F. Knoop, T. A. R. Purcell, M. Scheffler, and C. Carbogno, Anharmonicity measure for materials, Phys. Rev. Mater. **4**, 083809 (2020).
[30] F. Knoop, T. A. R. Purcell, M. Scheffler, and C. Carbogno, Fhi-vibes: *Ab initio* vibrational simulations, J. Open Source Software **5**, 2671 (2020).
[31] D. West and S. K. Estreicher, First-principles calculations of vibrational lifetimes and decay channels: Hydrogen-related modes in Si, Phys. Rev. Lett. **96**, 115504 (2006).
[32] M. T. Dove, *Introduction to Lattice Dynamics*, Cambridge Topics in Mineral Physics and Chemistry (Cambridge University Press, Cambridge, England, 1993), 10.1017/CBO9780511619885.
[33] A. Tkatchenko and M. Scheffler, Accurate molecular van der Waals interactions from ground-state electron density and free-atom reference data, Phys. Rev. Lett. **102**, 073005 (2009).
[34] T. Thonhauser, V. R. Cooper, S. Li, A. Puzder, P. Hyldgaard, and D. C. Langreth, Van der Waals density functional: Self-consistent potential and the nature of the van der Waals bond, Phys. Rev. B **76**, 125112 (2007).
[35] K. Hermann, Periodic overlayers and moiré patterns: Theoretical studies of geometric properties, J. Phys. Condens. Matter **24**, 314210 (2012).
[36] E. N. Voloshina, Y. S. Dedkov, S. Torbrügge, A. Thissen, and M. Fonin, Graphene on Rh(111): Scanning tunneling and atomic force microscopies studies, Appl. Phys. Lett. **100**, 141 (2012).
[37] A. Artaud, L. Magaud, T. Le Quang, V. Guisset, P. David, C. Chapelier, and J. Coraux, Universal classification of twisted, strained and sheared graphene moiré superlattices, Sci. Rep. **6**, 25670 (2016).
[38] L. Zhao, K. T. Rim, H. Zhou, R. He, T. F. Heinz, A. Pinczuk, G. W. Flynn, and A. N. Pasupathy, Influence of copper crystal surface on the CVD growth of large area monolayer graphene, Solid State Commun. **151**, 509 (2011).
[39] T. Niu, M. Zhou, J. Zhang, Y. Feng, and W. Chen, Growth intermediates for CVD graphene on Cu(111): Carbon clusters and defective graphene, J. Am. Chem. Soc. **135**, 8409 (2013).
[40] P. Süle, M. Szendrő, C. Hwang, and L. Tapasztó, Rotation misorientated graphene moire superlattices on Cu(111): Classical molecular dynamics simulations and scanning tunneling microscopy studies, Carbon **7**, 1082 (2014).
[41] M. Schulzendorf, A. Hinaut, M. Kisiel, R. Jöhr, R. Pawlak, P. Restuccia, E. Meyer, M. C. Righi, and T. Glatzel, Altering the properties of graphene on Cu(111) by intercalation of potassium bromide, ACS Nano **13**, 5485 (2019).
[42] S. Weiß, D. Gerbert, A. Stein, A. K. Schenk, X. Yang, C. Brülke, R. Kremring, S. Feldmann, F. C. Bocquet, M. Gille, S. Hecht, M. Sokolowski, P. Tegeder, S. Soubatch, and F. S. Tautz, Dependence of the adsorption height of graphenelike

adsorbates on their dimensionality, Phys. Rev. B **98**, 075410 (2018).
[43] Y. Fukaya, S. Entani, S. Sakai, I. Mochizuki, K. Wada, T. Hyodo, and S. I. Shamoto, Spacing between graphene and metal substrates studied with total-reflection high-energy positron diffraction, Carbon **103**, 1 (2016).
[44] C. Gong, G. Lee, B. Shan, E. M. Vogel, R. M. Wallace, and K. Cho, First-principles study of metal-graphene interfaces, J. Appl. Phys. **108**, 123711 (2010).
[45] M. Vanin, J. J. Mortensen, A. K. Kelkkanen, J. M. Garcia-Lastra, K. S. Thygesen, and K. W. Jacobsen, Graphene on metals: A van der Waals density functional study, Phys. Rev. B **81**, 081408(R) (2010).
[46] T. Olsen, J. Yan, J. J. Mortensen, and K. S. Thygesen, Dispersive and covalent interactions between graphene and metal surfaces from the random phase approximation, Phys. Rev. Lett. **107**, 156401 (2011).
[47] T. Olsen and K. S. Thygesen, Random phase approximation applied to solids, molecules, and graphene-metal interfaces: From van der Waals to covalent bonding, Phys. Rev. B **87**, 075111 (2013).
[48] G. Giovannetti, P. A. Khomyakov, G. Brocks, V. M. Karpan, J. Van den Brink, and P. J. Kelly, Doping graphene with metal contacts, Phys. Rev. Lett. **101**, 026803 (2008).
[49] V. M. Karpan, G. Giovannetti, P. A. Khomyakov, M. Talanana, A. A. Starikov, M. Zwierzycki, J. Van den Brink, G. Brocks, and P. J. Kelly, Graphite and graphene as perfect spin filters, Phys. Rev. Lett. **99**, 176602 (2007).
[50] A. V. Sidorenkov, S. V. Kolesnikov, and A. M. Saletsky, Graphene on Cu(111) at the nonzero temperatures: Molecular dynamic simulation, Mod. Phys. Lett. B **31**, 7 (2017).
[51] M. J. Bedzyk and G. Materlik, Determination of the position and vibrational amplitude of an adsorbate by means of multiple-order x-ray standing-wave measurements, Phys. Rev. B **31**, 4110 (1985).
[52] D. P. Woodruff, Surface structure determination using x-ray standing waves, Rep. Prog. Phys. **68**, 743 (2005).
[53] I. Brown and J. D. Bunitz, The crystal structure of diazoaminobenzene copper(I), Acta Crystallogr. **14**, 480 (1961).
[54] A. Bondi, Van der Waals volumes and radii, J. Phys. Chem. **68**, 441 (1964).
[55] M. Schwarz, A. Riss, M. Garnica, J. Ducke, P. S. Deimel, D. A. Duncan, P. K. Thakur, T. L. Lee, A. P. Seitsonen, J. V. Barth, F. Allegretti, and W. Auwärter, Corrugation in the weakly interacting hexagonal-BN/Cu(111) system: Structure determination by combining noncontact atomic force microscopy and x-ray standing waves, ACS Nano **11**, 9151 (2017).
[56] R. J. Maurer, V. G. Ruiz, J. Camarillo-Cisneros, W. Liu, N. Ferri, K. Reuter, and A. Tkatchenko, Adsorption structures and energetics of molecules on metal surfaces: Bridging experiment and theory, Prog. Surf. Sci. **91**, 72 (2016).
[57] J. F. Dobson and J. Wang, Successful test of a seamless van der Waals density functional, Phys. Rev. Lett. **82**, 2123 (1999).
[58] J. Harl, L. Schimka, and G. Kresse, Assessing the quality of the random phase approximation for lattice constants and atomization energies of solids, Phys. Rev. B **81**, 115126 (2010).
[59] S. Lebègue, J. Harl, T. Gould, J. G. Ángyán, G. Kresse, and J. F. Dobson, Cohesive properties and asymptotics of the dispersion interaction in graphite by the random phase approximation, Phys. Rev. Lett. **105**, 196401 (2010).
[60] W. Liu, F. Maaß, M. Willenbockel, C. Bronner, M. Schulze, S. Soubatch, F. S. Tautz, P. Tegeder, and A. Tkatchenko, Quantitative prediction of molecular adsorption: Structure and binding of benzene on coinage metals, Phys. Rev. Lett. **115**, 036104 (2015).
[61] R. J. Maurer, V. G. Ruiz, and A. Tkatchenko, Many-body dispersion effects in the binding of adsorbates on metal surfaces, J. Chem. Phys. **143**, 102808 (2015).
[62] B. P. Klein, J. M. Morbec, M. Franke, K. K. Greulich, M. Sachs, S. Parhizkar, F. C. Bocquet, M. Schmid, S. J. Hall, R. J. Maurer, B. Meyer, R. Tonner, C. Kumpf, P. Kratzer, and J. M. Gottfried, Molecule-metal bond of alternant versus nonalternant aromatic systems on coinage metal surfaces: Naphthalene versus azulene on Ag(111) and Cu(111), J. Phys. Chem. C **123**, 29219 (2019).
[63] V. G. Ruiz, W. Liu, E. Zojer, M. Scheffler, and A. Tkatchenko, Density-functional theory with screened van der Waals interactions for the modeling of hybrid inorganic-organic systems, Phys. Rev. Lett. **108**, 146103 (2012).
[64] A. Tkatchenko, A. Ambrosetti, and R. A. Distasio, Interatomic methods for the dispersion energy derived from the adiabatic connection fluctuation-dissipation theorem, J. Chem. Phys. **138**, 074106 (2013).
[65] A. Ambrosetti, A. M. Reilly, R. A. Distasio, and A. Tkatchenko, Long-range correlation energy calculated from coupled atomic response functions, J. Chem. Phys. **140**, 508 (2014).
[66] J. Hermann and A. Tkatchenko, Density functional model for van der Waals interactions: Unifying many-body atomic approaches with nonlocal functionals, Phys. Rev. Lett. **124**, 146401 (2020).
[67] J. P. Perdew, K. Burke, and M. Ernzerhof, Generalized gradient approximation made simple, Phys. Rev. Lett. **77**, 3865 (1996).
[68] J. Heyd, G. E. Scuseria, and M. Ernzerhof, Hybrid functionals based on a screened Coulomb potential, J. Chem. Phys. **118**, 8207 (2003).
[69] B. Sohail, P. J. Blowey, L. A. Rochford, P. T. P. Ryan, D. A. Duncan, T. Lee, P. Starrs, G. Costantini, D. P. Woodruff, and R. J. Maurer, Donor—acceptor co-adsorption ratio controls the structure and electronic properties of two-dimensional alkali—organic networks on Ag(100), J. Phys. Chem. C **127**, 2716 (2023).
[70] R. J. Maurer, W. Liu, I. Poltavsky, T. Stecher, H. Oberhofer, K. Reuter, and A. Tkatchenko, Thermal and electronic fluctuations of flexible adsorbed molecules: Azobenzene on Ag(111), Phys. Rev. Lett. **116**, 146101 (2016).
[71] T. Chanier and L. Henrard, From carbon atom to graphene on Cu(111): An ab-initio study, Eur. Phys. J. B **88**, 1 (2015).
[72] P. Merino, M. Švec, A. L. Pinardi, G. Otero, and J. A. Martín-Gago, Strain-driven moiré superstructures of epitaxial graphene on transition metal surfaces, ACS Nano **5**, 5627 (2011).

[73] A. V. Sidorenkov, S. V. Kolesnikov, and A. M. Saletsky, Molecular dynamics simulation of graphene on Cu(111) with different Lennard-Jones parameters, Eur. Phys. J. B **89**, 220 (2016).
[74] R. Chen and P. Trucano, Comparisons of atomic thermal motions for graphite at 300 K based on x-ray, neutron, and phonon-spectrum data, Acta Crystallogr. Sect. A **34**, 979 (1978).
[75] Z. R. Robinson, P. Tyagi, T. R. Mowll, C. A. Ventrice, and J. B. Hannon, Argon-assisted growth of epitaxial graphene on Cu(111), Phys. Rev. B **86**, 235413 (2012).
[76] 10.17172/NOMAD/2023.12.19-2.